Bulletin of the Seismological Society of America, Vol. 96, No. 1, pp. 59–68, February 2006, doi: 10.1785/0120050108

# Surface Deformation Associated with the $M_w$ 6.4, 24 February 2004 Al Hoceima, Morocco, Earthquake Deduced from InSAR: Implications for the Active Tectonics along North Africa

by Ziyadin Cakir, Mustapha Meghraoui, Ahmet M. Akoglu, Nasser Jabour, Samir Belabbes, and Lahsen Ait-Brahim

**Abstract** We study the surface deformation associated with the 24 February 2004 Al Hoceima earthquake ($M_w$ 6.4) that recently affected the Rif Mountains of Morocco. The coseismic displacement field is mapped using synthetic aperture radar interferometry (InSAR) with the Envisat (ESA) satellite data acquired in the ascending and descending modes. Our analysis and modeling of InSAR data suggest that the earthquake is associated with a northwest–southeast-trending right-lateral, apparently blind strike-slip fault with a seismic moment reaching $6.8 \times 10^{18}$ N m. This result is in contrast with the north-northeast–south-southwest left-lateral fault mechanism inferred from the modeling of seismic waves. Thrust-and-fold structures of the Rif Mountains developed during the Tertiary period, but the recent significant seismic events and late-Quaternary deformation indicate east–west extension accommodated by north–south-trending normal and northwest–southeast- and northeast–southwest-trending conjugate strike-slip faults. The active deformation illustrates the fragmentation of the Rif Mountain range due to the Africa–Iberia collision and west-southwestward escape tectonics.

## Introduction

On 24 February 2004, Al Hoceima and the Rif Mountains of Morocco were struck, once again, by a large earthquake ($M_w$ 6.4), 10 years after the 26 May 1994 ($M_w$ 6.0) event (Fig. 1). Located along the Africa–Eurasia plate boundary in the western Mediterranean, the Rif Mountain range is a thrust-and-fold belt that experienced several moderate-to-large earthquakes of mainly strike-slip mechanism consistent with a north-northwest–south-southeast to northwest–southeast direction of plate convergence (DeMets *et al.*, 1990). Although the background seismicity is relatively high, seismogenic faults of this region are poorly known, and their contribution to the convergence movements at the plate boundary remains undetermined.

Focal-mechanism solutions of the mainshock from various sources are in good agreement and indicate a strike-slip mechanism with either a north-northeast–south-southwest-trending left-lateral fault or a northwest–southeast-trending right-lateral fault (Table 1). Field observations following the earthquake did not reveal any clear surface faulting associated with the earthquake. Instead, widespread fissures, joints, and landslides trending subparallel to the northeast–southwest left-lateral nodal plane were observed between the Beni Abdellah village to the south and Ajdir village to the north (Fig. 2). Preliminary field interpretations suggest that the surface breaks may represent the fault rupture at depth, and thus the earthquake is presumably associated with a left-lateral strike-slip fault, a similar situation as for the 1994 event (Ait Brahim, Nakhcha, *et al.*, 2004). However, distribution of aftershocks recorded by a temporary local seismic network (Dorbath *et al.*, 2005) shows two lineations of seismicity in the directions northwest–southeast and north-northeast–south-southwest, suggesting that the event might have been associated with multiple fault breaks (Ait Brahim, Nakhcha, *et al.*, 2004). Therefore, in the absence of clear coseismic faulting and related tectonic features within the epicentral area, neither aftershock distribution nor focal-mechanism solutions can resolve the geometry and earthquake rupture characteristics.

In this article we use synthetic aperture radar interferometry (InSAR) in order to determine the fault characteristics and seismic parameters of the 24 February 2004 earthquake. The analysis of ascending and descending radar images provides two sets of interferograms with clearly visible deformation lobes in the epicentral area. Furthermore, a unique model of rupture dislocation defines the coseismic rupture and related seismic characteristics. Finally, we discuss the implications of coseismic strike-slip ruptures within the Africa–Eurasia plate-boundary deformation zone.

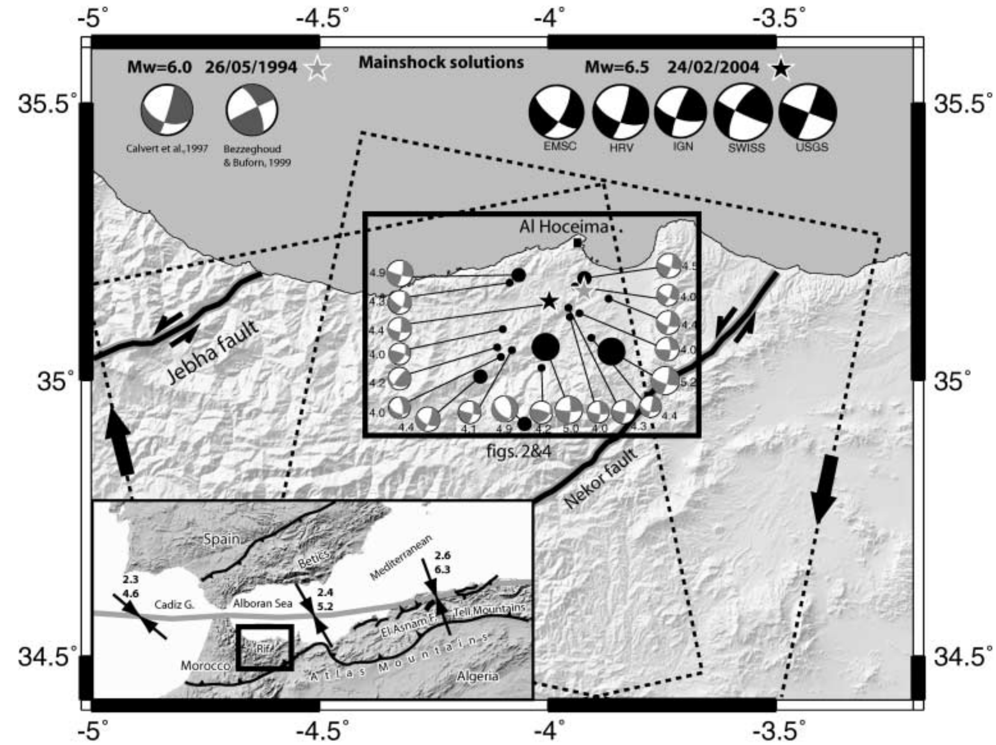


Figure 1. Al Hoceima region of Morocco with shaded relief (SRTM 90m). Large beach balls are focal-mechanism solutions of the 26 May 1994 and 24 February 2004 Al Hoceima earthquakes, whose epicenters are indicated by gray and black stars, respectively. Small black circles are $M > 4$ aftershocks of the 2004 earthquake from Instituto Geografico Nacional (IGN) with focal-mechanism solutions from Stich *et al.* (2005). Dashed rectangles are the frames of the Envisat radar images with arrows showing the flight direction of the satellite that looks to the right. The convergent plate boundary between Africa and Eurasia is depicted with a thick gray line in the inset map with arrows illustrating the direction of convergence (DeMets *et al.*, 1990; Nocquet and Calais, 2004).

## Tectonic Setting

The Rif region forms the westernmost mountain range of the east–west-trending thrust-and-fold system of North Africa and results mainly from the convergent movements of Africa toward Eurasia (Iberia) mainly during the Tertiary. The tectonic structures and compression regime of the Rif are comparable to the thrusts and nappes and related tectonic regime of the Tell Atlas mountain range in Algeria and Tunisia. From a global model of plate tectonics and GPS measurements combined with slip vectors of moderate-to-large earthquakes, DeMets *et al.* (1990), Pondrelli *et al.* (2002), McClusky *et al.* (2003), and Nocquet and Calais (2004) predict a range of 2.3–6.3 mm/yr northwest–southeast to north-northwest–south-southeast shortening between Africa and Eurasia in northern Morocco and Algeria, the Euler pole ranging between 2.1 and 21.0 in latitude and −20.0 and −18.3 in longitude. Although the driving force responsible for the active deformation along the plate boundary is the oblique convergence between the two plates, the pattern of seismicity is diffuse and varies significantly from east to west. In the long term, the rate of seismicity might be correlated with the rate of convergence along the plate boundary, but this is not evident to establish with the short period of instrumental seismic records. While the 1994 ($M_w$ 6.0) and 2004 ($M_w$ 6.4) moderate-to-large earthquakes and the recent seismicity manifest that the −400-km-long and 100-km-wide Rif Mountain range is being deformed under a strike-slip tectonic regime (Bezzeghoud and Buforn, 1999), adjacent regions in northern Algeria to the east and the Gulf of Cadiz to the west are subject to thrust faulting deformation (Grimison and Cheng, 1986). In their seismotectonic analysis, Meghraoui *et al.* (1996) suggest that the North African mountain ranges are the result of transpression tectonics that correspond to the interaction of shortening and transcurrent movements along the plate boundary. Paleoseismic investigations in northern Algeria (Meghraoui and Doumaz, 1996) and in southern Spain (Masana *et al.*, 2004) provide estimates of the total shortening ranging between 1.15 and 3.7 mm/yr along a N315 transect across the Betics and the Tell Atlas at the level of the El Asnam thrust-and-fold area. No such estimates of convergence rates have yet been determined across the Alboran Sea region.

Table 1
Focal-Mechanism Solutions of the 24 February 2004 Al Hoceima Earthquake

| | | | | Plane 1 | | | Plane 2 | | | |
|---|---|---|---|---|---|---|---|---|---|---|
| Source | Lon. | Lat. | Depth | Strike | Dip | Rake | Strike | Dip | Rake | $M_0$ (N m) |
| SED | −3.997 | 35.142 | 12.0 | 115 | 84 | 157 | 208 | 67 | 7 | $5.2 \times 10^{18}$ |
| HRV | −3.840 | 35.270 | 12.0 | 113 | 61 | −170 | 18 | 81 | −29 | $3.9 \times 10^{18}$ |
| IGN | −3.997 | 35.142 | 6.0 | 107 | 67 | 171 | 200 | 82 | 23 | $2.7 \times 10^{18}$ |
| IAG | −4.000 | 35.140 | — | 107 | 73 | −161 | 11 | 72 | −17 | $2.9 \times 10^{18}$ |
| USGS | −3.997 | 35.142 | 13.0 | 111 | 89 | −176 | 21 | 86 | −1 | $4.9 \times 10^{18}$ |
| EMSC | −4.000 | 35.000 | 29.0 | 128 | 69 | −158 | 30 | 69 | −23 | $3.6 \times 10^{18}$ |

SED: Swiss Seismological Service; HRV: Harvard; IGN: Instituto Geografico Nacional; IAG: Instituto Andaluz de Geofisica; EMSC: European–Mediterranean Seismological Centre.

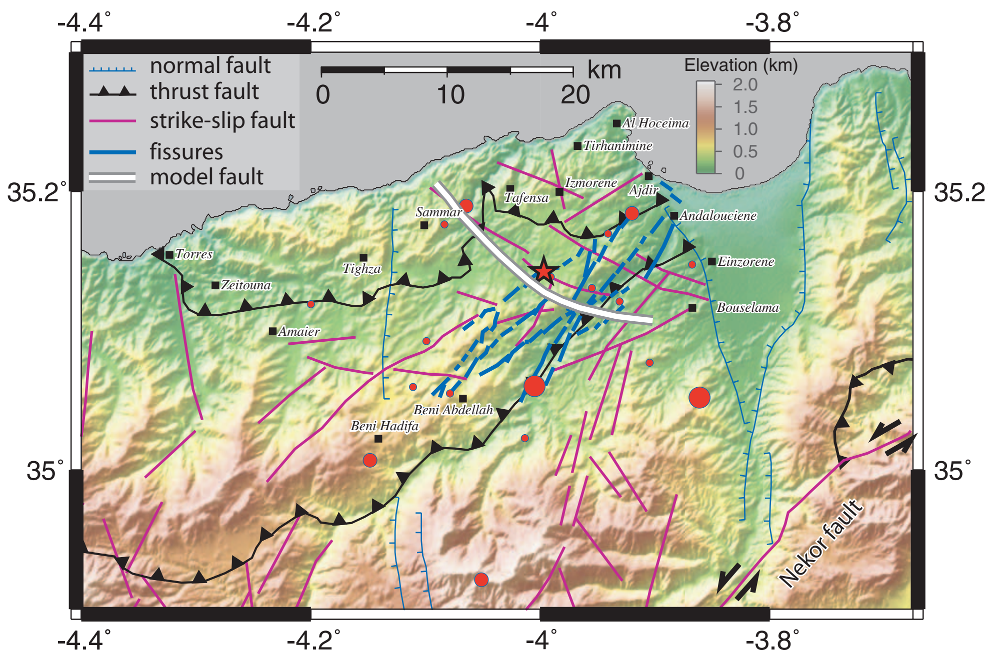


Figure 2. Tectonic map of the Al Hoceima region (compiled from Calvert *et al.*, 1997; Ait Ibrahim, Tadili, *et al.*, 2004) with surface cracks and fissures observed after the 2004 event (redrawn from Ait Brahim, Nakhcha, *et al.*, 2004). Red circles are the $M > 4$ aftershocks of the 2004 event whose epicenter is shown with a star (from IGN). Thick white line is the surface trace of the modeled fault plane.

The Al Hoceima region belongs to the east–west-trending imbricated thrust-and-fold system of the Rif Mountain range that results from the Tertiary tectonic regime (mostly Late Miocene and Lower Pliocene; Morel and Meghraoui, 1996). The neotectonic features of the Rif consist of the major Nekor and Jebha left-lateral strike-slip faults (Fig. 1), trending northeast–southwest, accompanied by north–south-trending normal faults that form a graben-like structure east of Al Hoceima and a conjugate network of relatively small (10–20 km long) northwest–southeast and northeast–southwest strike-slip faults (Fig. 2). The transpressive tectonics and existence of a complex fault network with thrust, normal, and strike-slip faulting in the Rif probably reflect the rapidly changing local tectonic regime with block rotations during the Neogene and Quaternary (Meghraoui *et al.*, 1996). Evidence of late Pleistocene and Holocene activity with typical prominent geomorphological features of seismogenic faulting is undocumented along the Rif neotectonic faults. Therefore, the identification of active and seismogenic faults in the Rif Mountains remains a difficult task that needs the contribution of new methods, including InSAR.

## Interferometric Data and Analysis

Over the last decade, InSAR has been proved to be a powerful tool for mapping crustal deformation due to earthquakes at a high spatial resolution with subcentimeter precision (Massonnet *et al.*, 1993); in addition, the InSAR methodology allows the measurements of postseismic relaxation, interseismic loading, and aseismic surface creep (Bürgmann *et al.*, 2000; Wright *et al.*, 2001; Fialko, 2004; Cakir *et al.*, 2005).

We use the European Space Agency's Envisat Advanced Synthetic Aperture Radar (ASAR) (Beam Mode 2) data acquired during ascending and descending passes of the satellite over the earthquake area in order to map the surface-deformation field (Fig. 1). Interferograms were calculated from ASAR Level-1 data (single look) using Doris InSAR processing software (Kampes *et al.*, 2003) with 1 range 5 azimuth looks (i.e., averaged to 20 × 20 m of ground pixel size) and precise satellite orbits from Delft University (Scharoo and Visser, 1998). Effects of topography were removed from the interferograms using the Shuttle Radar Topography Mission (SRTM) 3-arcsec posting digital elevation model (Farr and Kobrick, 2000).

We formed two ascending (track 230) and four descending (track 280) interferograms using nine ASAR images (Fig. 3). The best four interferograms are shown in Figure 4. Having the shortest temporal and spatial baseline, the ascending interferogram has the best coherence (Fig. 4a); decorrelation occurs due to large baselines, agricultural activities within the time span between image pairs (mainly descending pairs), and the steep slopes in the ragged terrain, particularly along the valley between Beni Abdellah and Einzorene (Figs. 2 and 4). The fact that there is no significant difference between the descending interferograms suggests that the atmospheric effects and orbital errors are negligible. The ascending interferograms show two asymmetric lobes of deformation with a peak-to-peak line-of-sight (LOS) displacement of about 23 cm (eight fringes), whereas three lobes of deformation can be seen in the descending interferograms with a maximum of five fringes (~12 cm) in the eastern lobe. While the two lobes in the coastal regions are clearly visible in all the interferograms, the southern lobe is somewhat obscured due to the poor coherence. The only common lobe between the ascending and descending interferograms is the one located immediately west of Al Hoceima.

Approximately 40% of east–west and 90% of vertical changes can be measured by synthetic aperture radar (SAR) interferometry with a steep look angle (−23° for Envisat Beam Mode 2 and European Remote Sensing [ERS] in the image center), whereas horizontal motion along the satellite flight direction that is approximately north–south but varies with latitude cannot be detected. Furthermore, a combination of horizontal and vertical displacement may lead to signal cancellation. Therefore, the striking difference in the fringe pattern between the ascending and descending interferograms mostly results from the change in the viewing geometry and the nature of surface deformation associated with a strike-slip fault trending oblique to the satellite flight direction. In the ascending and descending geometry, Earth surface is imaged from nearly opposite directions, and any changes in shape of the deformation reflect differences in the vertical versus horizontal deformation; the sum of ascending and descending interferograms is largely up motion, with about 10% of north motion, and the difference between the two phases (descending minus ascending) is approximately the east motion (Fielding *et al.*, 2005). Therefore, the surface displacement in the region where there is a common lobe between the ascending and descending interferograms must be overwhelmingly vertical (i.e., subsidence as it shows range increase).

## Modeling Interferograms

We utilize Poly3Dinv, a 3D-boundary element method that uses triangular dislocations in a linear-elastic and homogeneous half-space with a damped least-square minimization. Using triangular elements, one can reconstruct real-

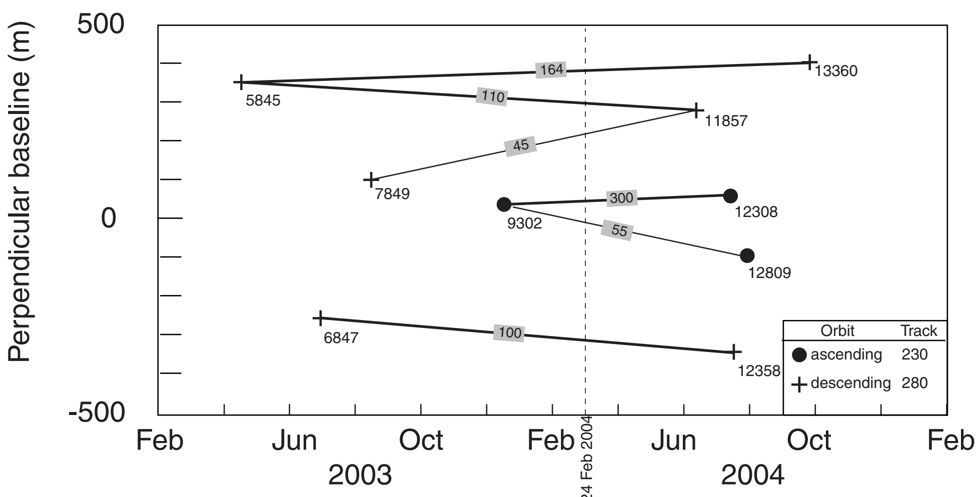


Figure 3. Baseline-time plot of the Envisat orbits used in this study. The elevation change that would produce an interferometric fringe (i.e., altitude of ambiguity), which depends on the interferometric baseline, is given in gray boxes. Interferograms shown in Figure 4 are produced using the interferometric pairs connected with bold lines.

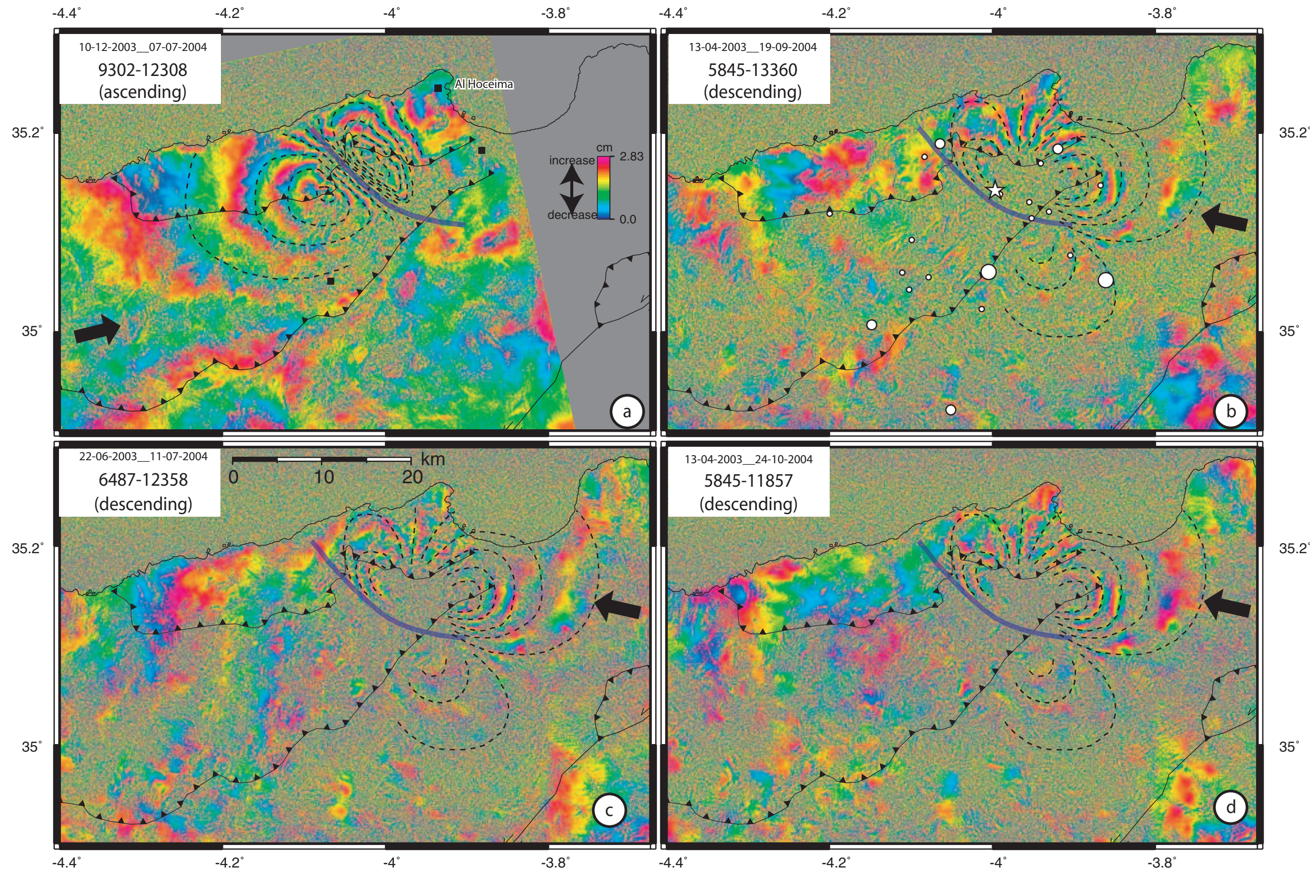


Figure 4. Coseismic Interferograms of the 24 February 2004 Al Hoceima earthquake. Each fringe shows 2.83 cm of surface displacement along the radar line of sight. Dashed lines are digitized fringes used in modeling the interferograms. Blue line is the best model fault. Barbed lines are inactive thrust faults shown to facilitate comparison of the interferograms. Black arrows indicate radar look direction.

istic fault surfaces, avoiding gaps and overlaps that are inevitably encountered when modeling curved or segmented faults of varying strike with rectangular dislocations commonly used to model geodetic observations. We used digitized fringes in our inversions instead of unwrapped data because some of the fringes that are readily visible could not be properly unwrapped due to the poor coherence to the south of the earthquake area (Thomas, 1995; Maerten *et al.*, 2005).

Since the fault rupture apparently did not reach the surface and the LOS component of the surface deformation captured by SAR interferometry is not quite unambiguous, we tested both northeast–southwest- and northwest–southeast-trending fault planes with varying dip and segmentation (i.e., single and multiple faults) (Table 2; Fig. 5). All the modeled faults used in our tests are discretized into triangular elements both along strike and azimuth (minimum 8 × 7 quadrangles, i.e., 112 triangles) so that realistic slip distribution can be obtained. Since the faults must not crosscut the visible fringes, northeast–southwest-trending left-lateral faults are placed only in areas of low coherence to the south of the earthquake area. The northwest–southeast-trending right-lateral strike-slip faults are placed along the fringe of zero LOS deformation between the two lobes of the ascending interferograms.

Modeling results indicate that the best fit to the ascending and descending interferograms can be achieved only by using a right-lateral strike-slip fault (Table 2, model 4B). As shown in Figure 5 and Table 2, each type of interferogram can presumably be modeled to some extent with left-lateral strike-slip faults, but with a significant difference in dip and strike—that is N15–20°E strike with near-vertical dip for the descending (model 1F) and N30–35°E with ~60° NW dip for the ascending interferograms (model 2E). While left-lateral faulting can adequately explain the descending interferograms, a satisfactory fit could not be obtained for the ascending ones, even with multiple faults of varying strike (model 3). This is because the ascending interferograms require unrealistically high (>5 m) slip on very short (5–10 km) faults located 7–10 km away from the lobe centers (i.e., areas of maximum LOS deformation; Fig. 4a). Therefore, a single or one type of interferogram (i.e., ascending or descending) should be interpreted with caution when deducing earthquake source parameters, especially in the absence of a clearly visible surface rupture.

Our best model fault is a curved right-lateral strike-slip

Table 2
Modeling Results with Varying Fault Kinematics and Geometry

| | | | | | RMS (cm) | | | | | |
|---|---|---|---|---|---|---|---|---|---|---|
| | | | | | Ascending | | Descending | | | |
| Model | Length (km) | Depth (km) | Azimuth (°) | Dip (°) | Alone | Joint | | Alone | $M_0$ (N m) | $M_w$ |
| 1A | 15 | 16.5 | 40 | 89 NW | — | 3.8 | 6.5 | — | $6.0 \times 10^{18}$ | 6.5 |
| 1B | 15 | 16.5 | 35 | 89 NW | — | 3.4 | 3.8 | — | $5.8 \times 10^{18}$ | 6.4 |
| 1C | 15 | 16.5 | 30 | 89 NW | — | 3.5 | 3.2 | — | $6.1 \times 10^{18}$ | 6.5 |
| 1D | 15 | 16.5 | 25 | 89 NW | — | 3.7 | 2.5 | — | $7.3 \times 10^{18}$ | 6.5 |
| 1E | 15 | 16.5 | 20 | 89 NW | — | 4.2 | 2.2 | — | $6.4 \times 10^{18}$ | 6.5 |
| 1F | 15 | 16.5 | 15 | 89 NW | — | 4.8 | 1.8 | 1.3 | $6.2 \times 10^{18}$ | 6.5 |
| 2A | 15 | 16.5 | 15 | 85 SE | — | 4.4 | 1.9 | — | $6.4 \times 10^{18}$ | 6.5 |
| 2B | 15 | 16.5 | 15 | 80 SE | — | 4.8 | 2.1 | — | $5.7 \times 10^{18}$ | 6.4 |
| 2C | 15 | 16.5 | 30 | 80 NW | — | 3.0 | 3.8 | — | $5.8 \times 10^{18}$ | 6.4 |
| 2D | 15 | 16.5 | 30 | 70 NW | — | 2.7 | 4.9 | — | $4.9 \times 10^{18}$ | 6.4 |
| 2E | 15 | 16.5 | 30 | 60 NW | 1.9 | 2.3 | 5.5 | — | $4.0 \times 10^{18}$ | 6.3 |
| 3A | 14 | 16.5 | 5–40 | 80 NW | — | 4.2 | 2.1 | — | $5.5 \times 10^{18}$ | 6.3 |
| 3B | 14 | 16.5 | 5–40 | 70 NW | — | 3.6 | 2.6 | — | $4.4 \times 10^{18}$ | 6.4 |
| 3C | 14 | 16.5 | 5–40 | 60 NW | — | 3.2 | 3.3 | — | $3.1 \times 10^{18}$ | 6.3 |
| 4A | 14 | 16.5 | 310 | 89 NE | — | 3.2 | 2.7 | — | $7.1 \times 10^{18}$ | 6.5 |
| 4B | 21 | 16.5 | 275–310 | 88 NE | — | 1.4 | 1.0 | — | $6.8 \times 10^{18}$ | 6.5 |

fault about 21 km long and 16.5 km wide, dipping 87–88° eastward with a strike changing from N85°W in the south to N50°W in the north (Fig. 6; Table 2). The excellent fit between the modeled and observed interferograms can be seen from the residual interferograms (i.e., models minus data) and profiles shown in Figure 6. The curved fault plane necessarily forms a restraining bend as the fault is associated with a right-lateral strike-slip movement. The location and the azimuth of the northwest–southeast-trending portion of the fault are well constrained, as we are forced to place the fault along the fringe of zero LOS deformation between the two lobes of the ascending interferograms (Fig. 4a). A change in the rupture strike along the southern fault section is required by both ascending and descending interferograms (Fig. 5d; Table 2). However, the presence of the poor coherence does not allow us to better constrain the location of the west-northwest–east-southeast-trending fault or to infer how the two rupture planes of different strikes are connected. We assume a continuous fault rupture with a bend, as it is a common feature along strike-slip faults.

The fault surface of the best model is composed of 14 and 8 quadrangles formed with a pair of triangles along azimuth and dip directions, respectively. Since the resolution of slip decreases with increasing depth, the size of the triangles is gradually increased (from 1 to 3 km) toward the bottom of the fault. The slip distribution on the fault was then inverted with a right-lateral constraint on the strike-slip component and zero displacement on the fault edges; no sign constraints were imposed on the dip-slip component. A smoothing operator is also applied to the inverted slip distribution; models with a less smoothing factor ($<0.3$) better predict the data but with unrealistically high and localized slips.

Our best slip model is shown in Figure 7. A large asperity with a predominant right-lateral displacement of up to 2.7 meters is present at a depth of 6–8 km on the west-northwest–east-southeast-trending portion of the fault to the south. The northwest–southeast-trending part of the fault to the north is dominated by oblique to normal slip, explaining the range increase indicated by the common lobe between the ascending and descending interferograms. The geodetic moment of $6.8 \times 10^{18}$ N m (equivalent of $M_w$ 6.5) determined from modeling is in good agreement with those obtained from seismological observations (Table 1).

The continuity of fringes across the northwest–southeast-trending portion of the fault in the ascending interferograms implies that the coseismic rupture did not reach the surface. Modeling suggests that the slip is practically absent in the uppermost ~2 km of the fault, which is also confirmed by the absence of aftershocks above 3 km of depth (Dorbath *et al.*, 2005). The depth of the coseismic slip along the west-northwest–east-southeast-trending part of the fault could not be well constrained owing to the poor coherence in this region. Therefore, the rupture could be shallower and thus some of the fissures of similar strike observed in the field might be directly linked with the earthquake rupture below (Ait Brahim, Nakheha, *et al.*, 2004). The presence of deep coseismic slip with large amplitudes suggests that the earthquake probably nucleated at depths below 8–10 km, which in turn may explain why the rupture did not break the surface. Another possible explanation for the superficial seismic slip is that the uppermost part of the brittle crust is detached as a result of imbricated thrust-and-nappes and thus has different mechanical properties. As proposed by Fialko *et al.* (2005), surface slip deficit may also result from a distributed inelastic deformation within the uppermost few kilometers of the Earth's crust, occurring predominantly during the interseismic period.

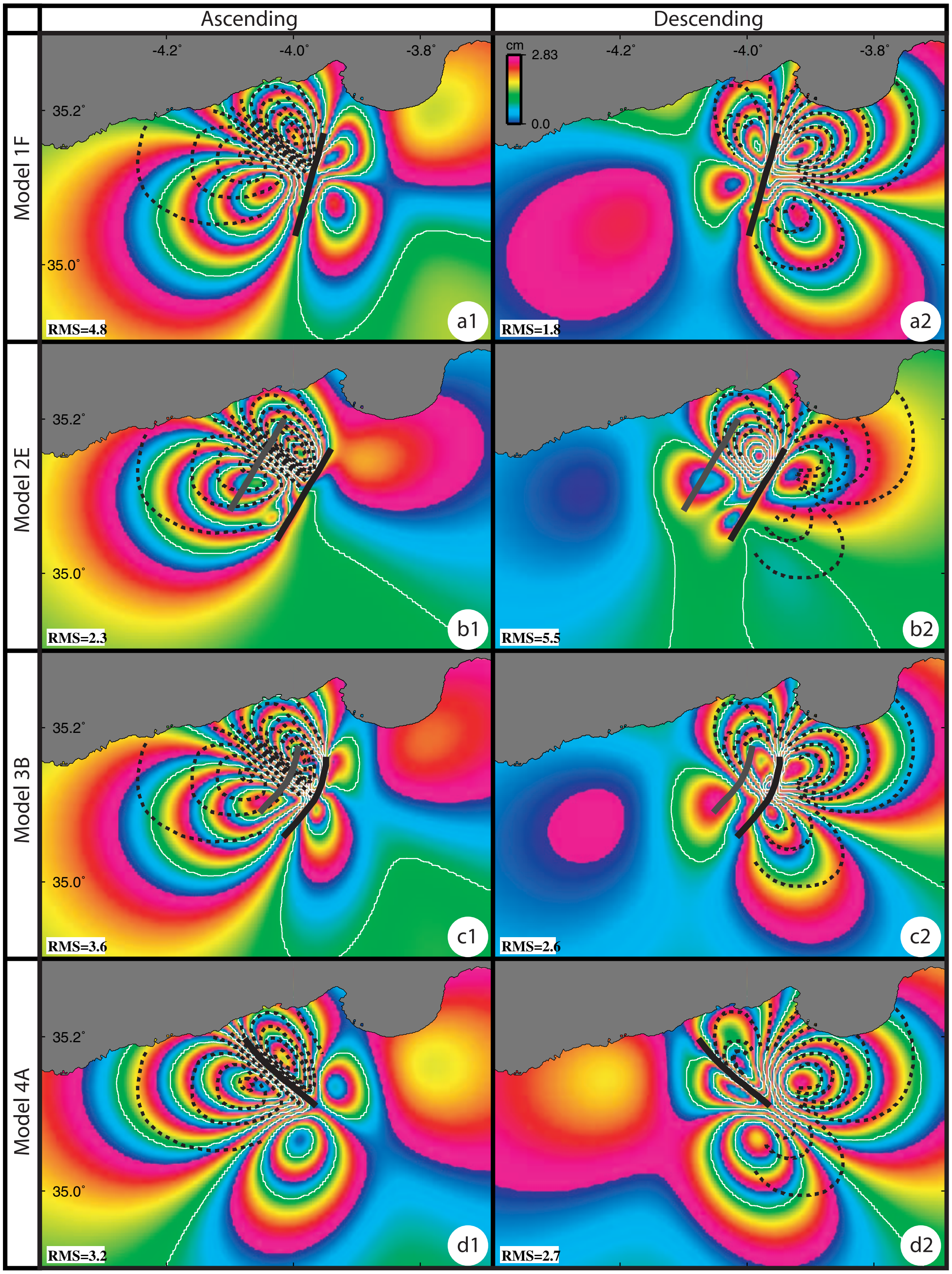


Figure 5. Synthetic interferograms obtained from joint inversion of ascending and descending data (digitized fringes, i.e., dashed lines) using modeled faults (black lines) with varying strike, dip, and mechanism (see Table 2 for details). (a) Planar and vertical fault with left-lateral slip. (b) Planar fault with 60° NW dip and left-lateral slip. (c) Curved fault with 70° NW dip and left-lateral slip. (d) Planar and vertical fault with right-lateral slip. Root mean square values are in centimeters.

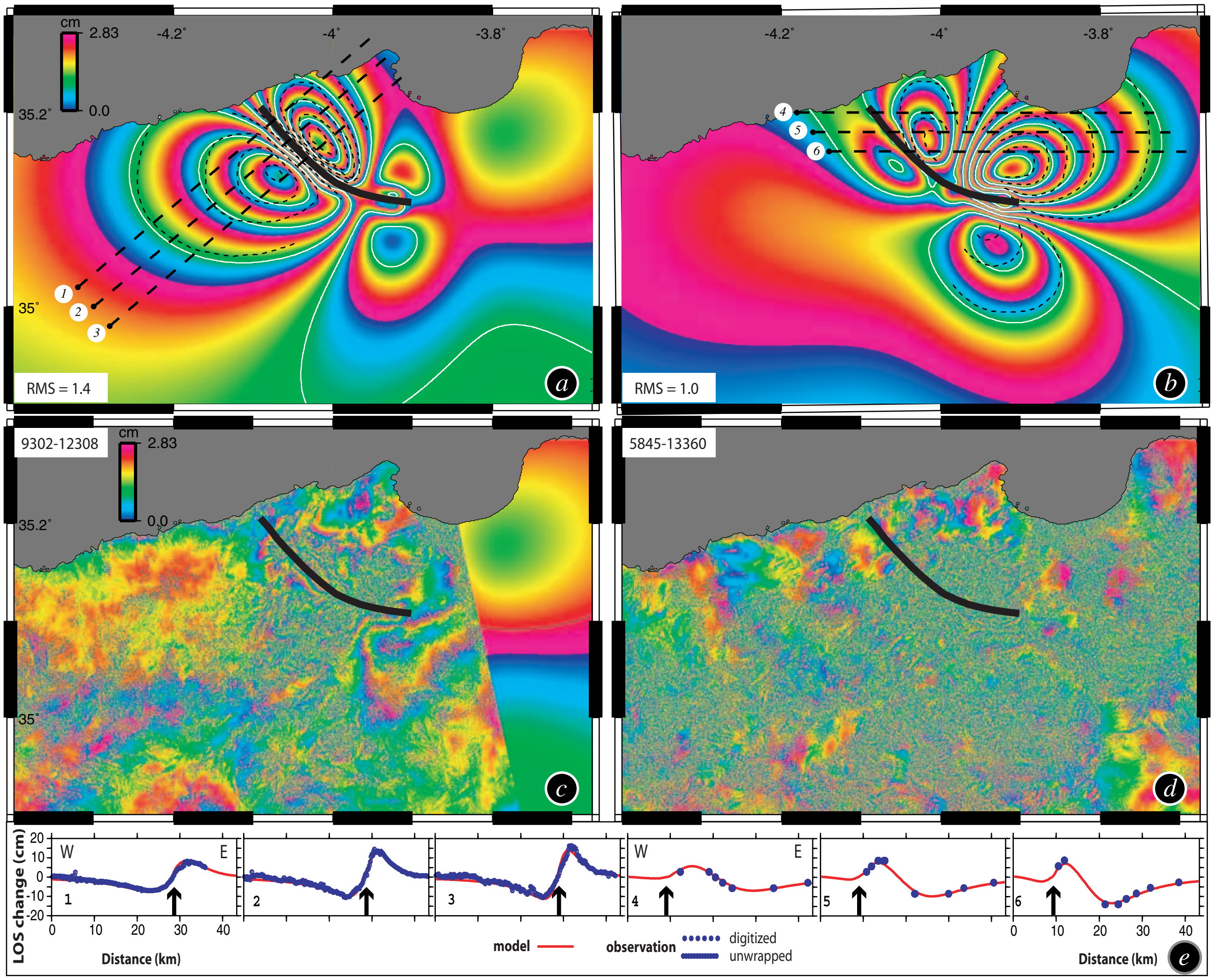


Figure 6. (a)–(b) Descending and ascending interferograms predicted by the best model (model 4B). (c)–(d) Two of the residual interferograms obtained after subtracting the synthetic interferograms from the observed data. (e) Line-of-sight profiles comparing the model with the data. Arrows show the position of the modeled fault.

## Discussion and Conclusions

Based on a detailed examination of Envisat radar data and subsequent modeling of the observed LOS surface deformation, we were able to determine the earthquake rupture parameters of the 24 February 2004 ($M_w$ 6.4) Al Hoceima earthquake. In the absence of surface faulting and complex aftershock distribution in a region like northern Morocco where morphology does not provide clear signals of active strike-slip faults, InSAR appears to be the appropriate methodology to characterize the seismic source parameters accurately and in detail.

The preferred northeast–southwest-trending left-lateral fault planes from seismologic studies based on regional and teleseismic waveform modeling (Buforn *et al.*, 2005) and apparent source time functions (ASTFs) (Stich *et al.*, 2005) are incompatible with the observed LOS surface deformation as they run north–south and N10°E. The InSAR near-field data analysis, particularly with both ascending and descending geometry, provides powerful constraints on the location and kinematics of the earthquake rupture. Any fault plane with a reasonable length and strike of north–south to N15°E cannot explain any of the coseismic interferograms, as it would crosscut the fringes through the deformation lobes. The waveform modeling or ASTF cannot distinguish between the two nodal planes of the double-couple source where both fault planes are plausible solutions. In the Al Hoceima case, taking into account the local tectonics and seismicity of the region, the left-lateral fault plane is preferred even though the right-lateral nodal plane fits ASTFs almost equally well (D. Stich, personal comm. 2005).

Previous studies of the aftershocks and intensity distribution (Calvert *et al.*, 1997; El Alami *et al.*, 1998; Bezzeghoud and Buforn, 1999) suggest that the May 1994 $M_w$ 6.0 earthquake took place on a north-northeast–south-southwest-trending left-lateral strike-slip fault. If this is correct,

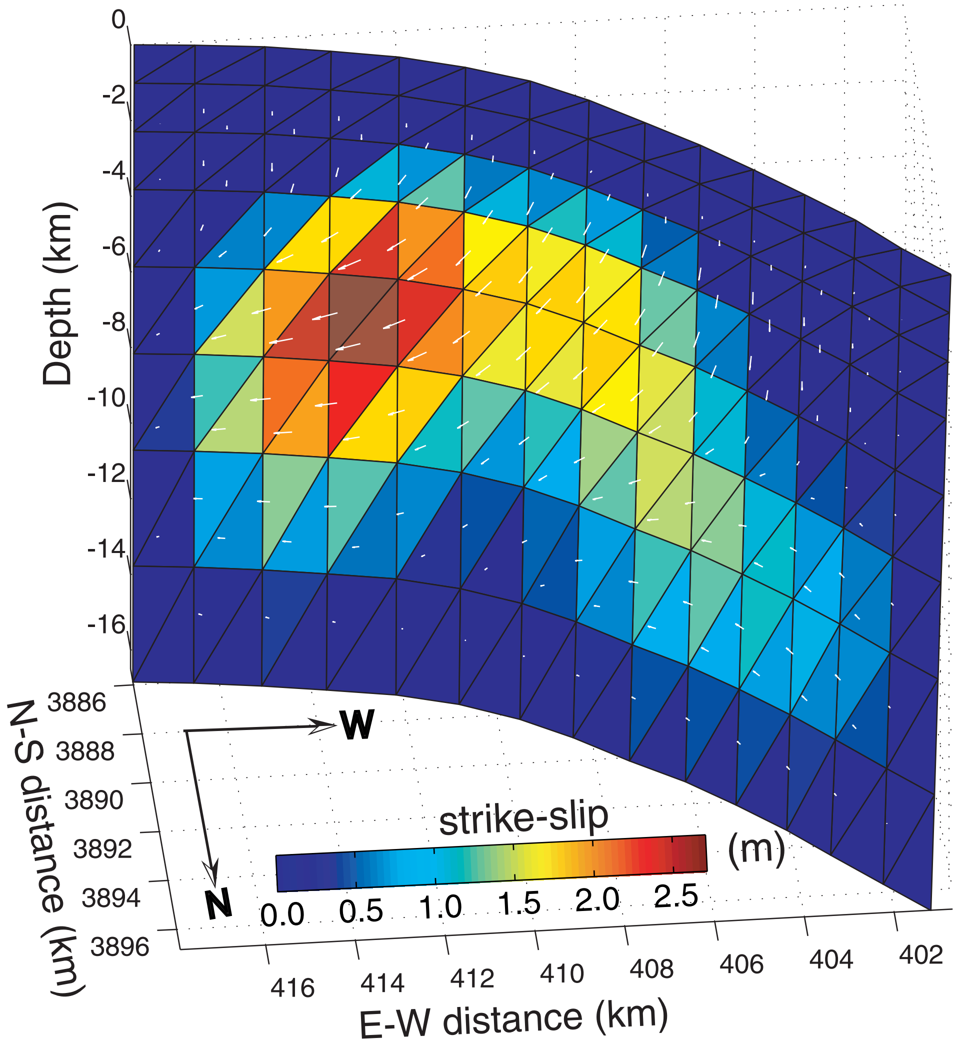


Figure 7. Strike-slip distribution on the modeled fault (model 4B). White arrows show the direction of motion of the eastern block relative to the western one (view toward southwest).

then the two earthquakes did not occur along the same fault but on conjugate faults.

Strike-slip earthquakes and related aftershocks with left- and right-lateral kinematics support the assumption that the Rif is subject to distributed strike-slip deformation via northwest–southeast- and northeast–southwest-trending conjugate faults. The Rif Mountain range can be considered a different and individual tectonic block along the plate boundary with respect to the Tell Atlas of Algeria that manifests earthquakes with noteworthy thrust kinematics (Meghraoui *et al.* 1996; Bezzeghoud and Buforn, 1999). That the active tectonics and related geomorphological features associated with strike-slip faults are not well developed on the landscape suggests that the Rif tectonic block is under the early stages of a new strike-slip regime. This observation is supported by the total absence of seismicity along (1) the graben-like structure and related prominent normal faults southeast of Al Hoceima, and (2) along the major Nekor strike-slip fault (Hatzfeld *et al.*, 1993). The relatively newly formed seismogenic strike-slip faults may explain the occurrence of moderate-sized earthquakes with $M_w$ <6.5. However, the northwest–southeast right-lateral faulting identified with InSAR is consistent with the oblique convergence and transpressive movements along the plate boundary and illustrates the complex rupture pattern and related seismicity of the Rif region.

## Acknowledgments

Envisat data are provided by the European Space Agency under CAT-1 project 2532. We thank Prof. David Pollard of Stanford University for providing us with the Poly3D software, in particular Frantz and Laurent Maerten for their support. We thank the associate editor R. Bürgmann and reviewers E. Price and F. Gomez for comments that improved the manuscript. Most of the figures were plotted using Genetic Mapping Tools (GMT) (Wessel and Smith, 1991). A.M.A. was supported by the EU FP6 TR-Access Mobility Project. This is the Institut de Physique du Globe (IPG) Strasbourg contribution No. 2005.03 UMR 7516.

## References

Ait Brahim, L., C. Nakhcha, B. Tadili, A. El Mrabet, and N. Jabour (2004). Structural analysis and interpretation of the surface deformations of the February 24th, 2004 Al Hoceima earthquake, *EMSC-Newsletter* **21,** 10–12.

Ait Brahim, L., B. Tadili, C. Nakhcha, I. Mouayn, M. Ramdani, M. Limouri, A. El Qadi, F. Sossey Alaoui, and M. Benhalima (2004). Modeling in the eastern Rif (northern Morocco) using active faults and seismicity for the strong motion, *Pure Appl. Geophys.* **161,** 1081–1091, 0033-4553/04/061081-11, doi 10.1007/s00024-003-2487-9.

Bezzeghoud, M., and E. Buforn (1999). Source parameters of the 1992 Melilla (Spain, $M_w$ 4.8), 1994 Alhoceima (Morocco, Mw 5.8) and 1994 Mascara (Algeria, $M_w$ 5.7) earthquakes and seismotectonic implications, *Bull. Seism. Soc. Am.* **89,** 359-372.

Buforn, E., M. Bezzeghoud, C. del Fresno, J. F. Borges, R. Madariaga, and A. Udías (2005). Study of the fracture process of Al Hoceima earthquake (24/02/2004, Mw = 6.2) from regional and teleseismic data, *Geophys. Res. Abst.* **7,** 05301, SRef-ID 1607-7962/gra/EGU05-A-05301.

Bürgmann, R., D. Schmidt, R. M. Nadeau, M. d'Alessio, E. Fielding, D. Manaker, T. V. McEvilly, and M. H. Murray (2000). Earthquake potential along the northern Hayward fault, California, *Science* **289,** 1178–1181.

Cakir, Z., A. M. Akoglu, S. Belabbes, S. Ergintav, and M. Meghraoui (2005). Creeping along the North Anatolian fault at Ismetpasa (western Turkey): rate and extent from InSAR, *Earth Planet. Sci. Lett.* **238,** 225–234.

Calvert, A., F. Gomez, D. Seber, M. Barazangi, N. Jabour, L. Ait Brahim, and A. Demnati (1997). An integrate geophysical investigation of recent seismicity in the Al-Hoceima region of north Morocco, *Bull. Seism. Soc. Am.* **87,** 637–651.

DeMets, C., R. G. Gordon, D. F. Argus, and S. Stein (1990). Current plate motions, *Geophys. J. Int.* **101,** 425–478.

Dorbath, L., Y. Hahou, B. Delouis, C. Dorbath, J. Van Der Woerd, S. Bardrane, M. Frogneux, H. Haessler, E. Jacques, M. Menzhi, and P. Tapponnier (2005). Études sismologiques sur le séisme D'al Hoceima: localisation, et mécanisme du choc principal et des répliques, contraintes et structure de la zone epicentrale. Presented at Colloque Intenational Seisme d'Al Hoceima: bilan et perspectives, 24–26 February 2005, Al Hoceima, Morocco.

El Alami, S. O., B. Tadili, T. E. Cherkaoui, F. Medina, M. Ramdani, L. Ait Brahim, and M. Harnafi (1998). The Al Hoceima earthquake of May 26, 1994 and its aftershocks: a seismotectonic study, *Annali di Geofisica* **41,** no. 4, 519–537.

Farr, T., and M. Kobrick (2000). Shuttle radar topography mission produces a wealth of data, *EOS Trans. AGU* **81,** 583–585.

Fialko, Y. (2004). Evidence of fluid-filled upper crust from observations of postseismic deformation due to the 1992 Mw 7.3 Landers earthquake, *J. Geophys. Res.* **109,** B08401, doi 10.1029/2004JB002985.

Fialko, Y., D. Sandwell, M. Simons, and P. Rosen (2005). Three-dimensional deformation caused by the Bam, Iran, earthquake and the origin of shallow slip deficit, *Nature* **435,** doi 10.1038/nature03425.

Fielding, E. J., M. Talebian, P. A. Rosen, H. Nazari, J. A. Jackson, M. Ghorashi, and R. Walker (2005). Surface ruptures and building damage of the 2003 Bam, Iran, earthquake mapped by satellite synthetic aperture radar interferometric correlation, *J. Geophys. Res.* **110,** B03302, doi 10.1029/2004JB003299.

Grimison, N., and W. Cheng (1986). The Azores–Gibraltar plate boundary: focal mechanisms, depths of earthquakes and their tectonic implications, *J. Geophys. Res.* **91,** 2029–2047.

Hatzfeld, D., V. Caillot, T.-E. Cherkaoui, H. Jebli, and F. Medina, (1993). Microearthquake seismicity and fault plane solutions around the Nekor strike-slip fault, Morocco, *Earth Planet. Sci. Lett.* **120,** 31–41.

Kampes, B., R. Hanssen, and Z. Perski (2003). Radar interferometry with public domain tools, in *Proceedings of FRINGE 2003*, 1–5 December, Frascati, Italy.

Maerten, F., P. G. Resor, D. D. Pollard, and L. Maerten (2005). Inverting for slip on three-dimensional fault surfaces using angular dislocations, *Bull. Seism. Soc. Am.* **95,** 1654–1665.

Masana, E., J. J. Martínez-Díaz, J. L. Hernández-Enrile, and P. Santanach (2004). The Alhama de Murcia fault (SE Spain), a seismogenic fault in a diffuse plate boundary: seismotectonic implications for the Ibero-Magrebian region, *J. Geophys. Res.* **109,** B01301, doi 10.1029/2002JB002359.

Massonnet, D., M. Rossi, C. Carmona, F. Adragna, G. Peltzer, K. Feigl, and T. Rabaute (1993). The displacement field of the Landers earthquake mapped by radar interferometry, *Nature* **364,** 138–142.

McClusky, S., R. Reilinger, S. Mahmoud, D. Ben Sari, and A. Tealeb (2003). GPS constraints on Africa (Nubia) and Arabia plate motions, *Geophys. J. Int.* **155,** 126–138, doi 10.1046/j.1365-246X.2003.02023.

Meghraoui, M., and F. Doumaz (1996). Earthquake-induced flooding and paleoseismicity of the El Asnam (Algeria) fault-related fold, *J. Geophys. Res.* **101,** 17,617–17,644.

Meghraoui, M., J. L. Morel, J. Andrieux, and M. Dahmani (1996). Tectonique plioquaternaire de la chaîne tello-rifaine et de la mer d'Alboran; Une zone complexe de convergence continent, *Bulletin Societe Geologique de France* **167,** no. 1, 141–157.

Morel, J. L., and M. Meghraoui (1996). The Goringe-Alboran-Tell (GALTEL) tectonic zone, a transpression system along the Africa-Eurasia plate boundary, *Geology* **24,** 755–758.

Nocquet, J.-M., and E. Calais (2004). Geodetic measurements of crustal deformation in the western Mediterranean and Europe, *Pure Appl. Geophys.* **161,** 661–681, 0033-4553/04/030661-21, doi 10.1007/s00024-003-2468.

Pondrelli, S., A. Morelli, G. Ekström, S. Mazza, E. Boschi, and A. M. Dzlewonski (2002). European-Mediterranean regional centroid-moment tensors: 1997–2000, *Phys. Earth Planet. Interiors* **130,** 71–101.

Scharoo, R., and P. Visser (1998). Precise orbit determination and gravity field improvement for the ERS satellites, *J. Geophys. Res.* **103,** 8113–8127.

Stich, D., F. de Lis Mancilla, D. Baumont, and J. Morales (2005). Source analysis of the 6.3, 2004, Al Hoceima earthquake (Morocco) using regional apparent source time functions, *J. Geophys. Res.* **110,** B6, B06306, doi 10.1029/2004JB003381.

Thomas, A. L. (1995). Poly3D: a three-dimensional, polygonal element, displacement discontinuity boundary element computer program with applications to fractures, faults, and cavities in the earth's crust, *Master's Thesis*, Stanford University, 221 pp.

Wessel, P., and W. H. F. Smith (1991). Free software helps map and display data, *EOS Trans. AGU* **72,** 441, doi 10.1029/90EO00319, 1991.

Wright, T. J., B. Parsons, and E. J. Fielding (2001). Measurement of interseismic strain accumulation across the North Anatolian fault by satellite radar interferometry, *Geophys. Res. Lett.* **28,** 2117–2120.

EOST—Institut de Physique du Globe
5, rue René Descartes
67084 Strasbourg Cedex, France
ziyadin.cakir@eost.u-strasbg.fr
(Z.C., M.M., S.B.)

Eurasian Institute of Earth Sciences ITU
Istanbul, Turkey
(A.M.A.)

Laboratoire de Geophysique
CNRST
Rabat, Morocco
(N.J.)

des Sciences de la Terre
Universite Mohammed V
Morocco
(L.A.-B.)

Manuscript received 27 May 2005.